ORIGINAL ARTICLE

Pawel Zochowski [ID] · **Marcin Cegła** [ID] · **Krzysztof Szczurowski** [ID] · **Jędrzej Mączak** [ID] ·
Marcin Bajkowski [ID] · **Ewa Bednarczyk** [ID] · **Roman Grygoruk** [ID] · **Mariusz Magier** [ID] ·
Dariusz Pyka [ID] · **Mirosław Bocian** [ID] · **Krzysztof Jamroziak** [ID] · **Roman Gieleta** [ID] ·
Piotr Prasuła [ID]

Experimental and numerical study on failure mechanisms of the 7.62 × 25 mm FMJ projectile and hyperelastic target material during ballistic impact

P. Zochowski · M. Cegła
Military Institute of Armament Technology, Prym. S. Wyszynskiego 7, 05-220 Zielonka, Poland
E-mail: zochowskip@witu.mil.pl

M. Cegła
E-mail: ceglam@witu.mil.pl

K. Szczurowski · J. Mączak
Institute of Vehicles, Faculty of Automotive and Construction Machinery Engineering, Warsaw University of Technology, Narbutta 84, 02-254 Warsaw, Poland
E-mail: krzysztof.szczurowski@pw.edu.pl

J. Mączak
E-mail: jedrzej.maczak@pw.edu.pl

M. Bajkowski · E. Bednarczyk · R. Grygoruk · M. Magier (✉)
Institute of Mechanics and Printing, Faculty of Mechanical and Industrial Engineering, Warsaw University of Technology, Narbutta 85, 02-524 Warsaw, Poland
E-mail: mariusz.magier@pw.edu.pl

M. Bajkowski
E-mail: marcin.bajkowski@pw.edu.pl

E. Bednarczyk
E-mail: ewa.bednarczyk@pw.edu.pl

R. Grygoruk
E-mail: roman.grygoruk@pw.edu.pl

D. Pyka · M. Bocian · K. Jamroziak
Department of Mechanics, Materials and Biomedical Engineering, Faculty of Mechanical Engineering, Wroclaw University of Science and Technology, Smoluchowskiego 25, 50-370 Wroclaw, Poland
E-mail: dariusz.pyka@pwr.edu.pl

M. Bocian
E-mail: miroslaw.bocian@pwr.edu.pl
at K. Jamroziak E-mail: krzysztof.jamroziak@pwr.edu.pl

R. Gieleta
Institute of Mechanics and Computational Engineering, Faculty of Mechanical Engineering, Military University of Technology, Kaliskiego 2, 00-908 Warsaw, Poland
E-mail: roman.gieleta@wat.edu.pl

P. Prasuła
Doctoral School No. 1, Faculty of Chemistry, Warsaw University of Technology, Noakowskiego 3, 00-664 Warsaw, Poland
E-mail: 00247264@pw.edu.pl

Abstract The main aim of the work was the experimental and numerical analysis of the energy absorption/dissipation capabilities and failure mechanisms of novel hyper-elastic target material intended for ballistic applications including layers of composite armors, projectile catching systems and anti-ricochet layers covering walls of shooting ranges, ballistic tunnels, etc. Static and dynamic mechanical properties of the material were analyzed at both room and elevated temperatures ($40 \div 80\,°C$). Numerical models of the material and 7.62×25 mm FMJ projectile were defined. Simulations of the hyper-elastic target penetration with the projectile were carried out. The differences between the results obtained numerically and experimentally were determined (measured as a relative error) and were lower than 15% what testified about proper definition of the numerical models of the analyzed phenomenon components.

1 Introduction

Hyper-elastic rubber-like materials are commonly used in various branches of engineering, especially in those applications where high damping properties are required [1–4]. In recent years, there were many attempts to use relatively soft hyperelastic rubber-like materials as well as non-Newtonian materials, shear-thickening and magnetorheological fluids or additively manufacturing pantographic structures, in various ballistic applications [5–17]. Obviously, these materials cannot constitute a standalone armors, but their advantages such as relatively low cost, durability even under multiple impact conditions, high recycling capacity, energy absorption and dissipation capabilities make them interesting option that can be used in composite armors applications as interlayers in multilayered designs, adhesive joints, spall liners, etc., to enhance the efficiency of such solutions. For example in the work [18], authors improved the protection capability of rubber-metal armor systems by around 8% by optimizing rubber interlayer (proper adjustment of parameters such as hardness, damping, glass transition temperature). The protection effectiveness of high hardness steel subjected to penetration by projectiles was increased by use of elastomeric coatings in the work [19]. In that case, the large difference in impedance between target materials was indicated as a main factors of efficiency enhancement. The authors indicated that appropriate bending stiffness of the backing material is crucial for proper functioning of the elastomer. In the work [20], butyl-rubber was used in the form of floor mats protecting occupants against potential injuries from under vehicle blast loading [21]. Rubber layers are often used in non-explosive reactive armors (NERA) protecting against kinetic-energy penetrators (KEP), long-rod projectiles [22–24] and shaped charge jets [25–28]. In such armors, elastomers or polymers are placed between steel plates. Protective mechanisms in such solutions are based mainly on the bulging effect. For example in the work [29], author proved that bulging effect in the laminated steel-elastomer armor disturbed and slendered KEP projectiles, causing their fragmentation.

Ballistic applications of hyperelastic rubber-like materials include also human tissue simulants in analyses of different types of ballistic trauma. Experiments on human or animal cadavers are difficult to carry out due to both practical and ethical issues. Therefore, scientists were enforced to develop new types of homogeneous materials that could substitute human tissues or their conventional simulants (ballistic gelatins [30,31], ballistic soaps [32,33]) used in both penetrating [34,35] and blunt [36,37] ballistic impact scenarios. Moreover, other than soft materials, a mention can be made of the result of an impact toward stiffer living tissue as bone [38,39]. Using of gelatins in ballistic impact experiments may be unconvenient due to their temperature sensitivity, and temporal character of cavities produced by penetrating projectile [40,41]. For those reasons, synthetic equivalents of conventional gelatins and soaps were developed (SEBS—styrene-ethylene-butylene-styrene gel, Perma-Gel®—styrene-ethylene-butylene co-polymer, Sylgard gel, etc.). Synthetic tissue simulants have numerous benefits in relation to conventional ones, such as low temperature sensitivity, transparency and uniform mechanical properties [42,43]. They can be recast after testing and do not suffer from biological degradation. Efficiency of hyperelastic tissue simulants was confirmed in numerous studies of ballistic impact phenomenon. In the work [44], authors carried out a series of tests in which the ballistic response of Perma-Gel®to the impact of ball bearings with a diameter of 5.5 mm and impact velocities of between 150 and 1050 m/s was analyzed. Efficiency of the material was compared directly to that of 10% and 20% gelatin. Comparison of depths of penetration values in Perma-Gel®and gelatin targets showed reasonable agreement. The indentation response of Perma-Gel was investigated also in the work [45]. Analysis of indentation depths showed that Perma-Gel properly reproduced real tissue response, especially at low strain energy densities.

Fig. 1 The hyperelastic rubber-like target material

Lower correlation was achieved as the loading mass increased. Mechanical properties of SEBS gel were analyzed in a wide range of strain rates in the work [46]. Barreling effect and a non-homogeneous radial strain of the sample were observed during compression experiments what caused that material behavior was not identified for a whole range of strain through mechanical testing. The study of thermic effects can be faced from a modeling point of view introducing a more comprehensive thermo-viscoelastic model as done in [47]. With the same spirit, namely using a variational approach, plasticity, friction, and damage effects could be taken into account; see, e.g., [48–53]. The others investigations of new innovative armors, light and practical, could be framed in the design of new metamaterials, see [54,55].

Ballistic tests are highly dynamic and destructive phenomena that are very difficult to analyze and quantitative assessment, especially when hyper-elastic materials are included. Such materials can significantly deform under mechanical load, but their deformations are temporary—they exhibit high elastic recovery and nonlinear stress–strain-deformation relationship in the deformation range above 5%. That is why the ballistic experiments on rubber-like materials are often supported by numerical methods allowing to obtain additional information about phenomena. For example in the paper [56], a new visco-hyperelastic law based on the Mooney–Rivlin model was proposed to numerically reproduce the SEBS gel material behavior. The material characterization tests were performed over a wide range of strain rates (0.002–$1500\,\mathrm{s}^{-1}$). Sylgard gel and ballistic gelatin under ballistic impact were modeled with Mooney–Rivlin and Ogden material models in the works [57,58] and [59], respectively.

The main aim of the present study was to create an accurate and verified constitutive model of novel hyperelastic material that will be able to facilitate designing processes of various types of protective structures used in different ballistic applications including layers of composite armors, projectile catching systems and anti-ricochet layers covering walls of shooting ranges, ballistic tunnels, etc.

2 Materials

The novel hyper-elastic material analyzed in the study is an elastomer based on modified silicones. The density of the material (determined as an average of three measurements) was $946\,\mathrm{kg/m^3}$. The using temperature ranges from about –20 ° to + 60 °C (Fig. 1).

The hyper-elastic material constituted a target that was impacted with 7.62×25 mm full metal jacket (FMJ) bullet (NIJ level I and IIA) [60]. The bullet core is made of lead-antimony alloy and is surrounded with a tombac covered steel jacket (Fig. 2). The initial velocity of analyzed variant of projectile was around 420 m/s what gives the energy of about 550–600 J (mass $m = 5.5$ g).

3 Materials characterization tests

In the current study, the material type *MAT_181_SIMPLIFIED_RUBBER in LS-DYNA software [61,62] was chosen to describe the hyperelastic behavior of target material since it does not require parameter fitting procedure like in classic Ogden or Yeoh models. Instead of this, the experimental curves of engineering stress
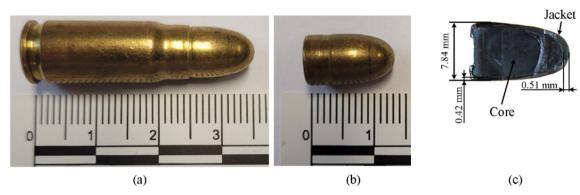
Fig. 2 The 7.62× 25 mm cartridge with the FMJ projectile: **a** cartridge, **b** projectile, **c** projectile cross section
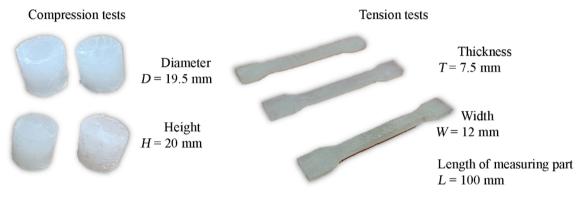

Fig. 3 Samples prepared for quasi-static mechanical tests

in function of engineering strain constitute the main input to the model. The curves should cover the complete range of expected response, including both compressive (negative values) and tensile (positive values) regimes.

3.1 Quasi-static compression tests

Compression and tension tests were carried out on the samples showed in Fig. 3 in order to collect data (force-displacement curves) allowing subsequent definition and validation of numerical models of the target material by numerical reproduction of experimental tests and comparison the results obtained in simulations with the experimental observations. Camera was used to register deformation of samples and to measure their actual cross sections.

Zwick Z100 universal testing machine with a hydraulic drive was used for mechanical experiments (Fig. 4).

The compression and tension processes registered with a camera are shown in Figs. 5 and 6, respectively.

The results of quasi-static compression tests of the target material at room temperature are shown in Fig. 7. The analyzed hyperelastic material showed a slight resistance ($\sigma_{eng} < 10$ MPa) to the testing machine punch, up to a deformation of about 70%. Then, the registered stresses started to increase exponentially, which, however, was caused by the accelerating flattening of the material (probably breaking of the internal bonds between the chains) and the decrease in the distance between the punches of the testing machine.

Similarly, in the case of tensile tests, where the stress in the material did not exceed the value of $\sigma_{eng} < 2.5$ MPa (Fig. 8). In this case, it should be noted that the failure strain of the material was approximately 160% (Figs. 6, 8).

3.2 Dynamic compression of hyperelastic target material.

Split Hopkinson Pressure Bar (SHPB) apparatus was used for dynamic compression of hyper-elastic material samples (Fig. 9) [63–65]. The load pulse was shaped with a copper disk 5 mm in diameter and 3 mm thick.
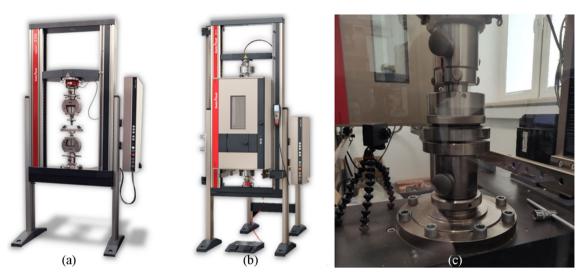
Fig. 4 Stand for material characterization tests: **a** Zwick Z100 testing machine, **b** machine equipped with temperature chamber, **c** compressed sample

$t = 0$ s, $L = 0$ mm $t = 9$ s, $L = 3$ mm, $t = 18$ s, $L = 6$ mm

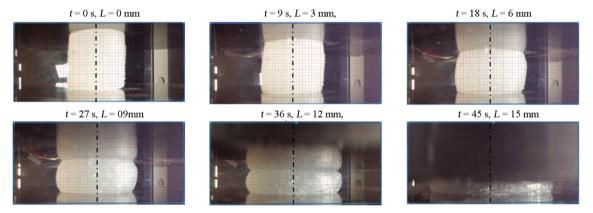$t = 27$ s, $L = 09$ mm $t = 36$ s, $L = 12$ mm, $t = 45$ s, $L = 15$ mm

Fig. 5 Quasi-static compression of hyper-elastic sample

As shown in Fig. 10, the results obtained in tests with the use of SHPB are characterized by a very large dispersion. In addition, the stress levels recorded in the samples reached values close to 100 MPa, which would suggest strain rate hardening of the material exceeding 1000%. Therefore, these results were unreliable and such a large error could be caused by some mistake in the recording of signals from the bars or the inhomogeneity of the samples and the occurrence of air bubbles inside of them. Therefore, the results from the SHPB tests were not used to determine the strain rate sensitivity of the material. The strain-hardening of the material was determined in a simplified manner by applying appropriate multipliers.

For this purpose, the stress–strain curves obtained during quasi-static tests and the results of ballistic tests determining the dependence of the residual velocity of the projectile on the thickness of the perforated target made of a hyperelastic material were used. Ballistic experiments were reproduced numerically. In order to determine the proper course of the curves for the material under dynamic conditions for a known strain rate, the stresses and strains recorded in quasi-static tests were multiplied and divided, respectively, by the appropriate values of coefficient in such a way as to obtain the residual velocity of the projectile similar like those recorded in experiments.

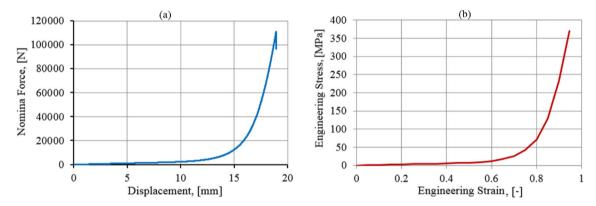**Fig. 6** Quasi-static tension of hyper-elastic sample

Fig. 7 Curves plotted on the basis of quasi-static compression tests of the hyper-elastic material at room temperature
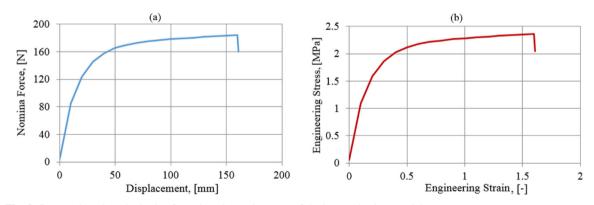

Fig. 8 Curves plotted on the basis of quasi-static tension tests of the hyper-elastic material at room temperature
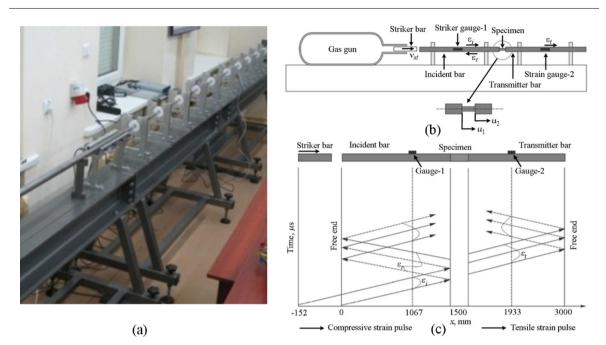
Fig. 9 Stand for dynamic compression of hyper-elastic sample: **a** Hopkinson bar system, **b** scheme of the Hopkinson bar stand; **c** wave propagation course [63]
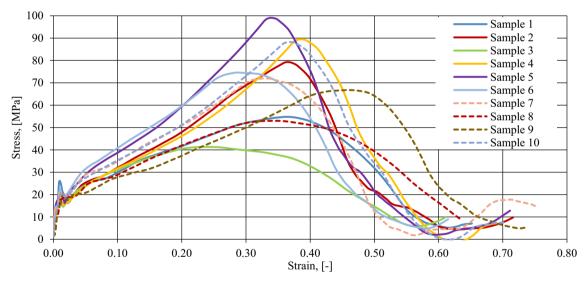

Fig. 10 Curves plotted on the basis of dynamic compression tests

3.3 Material characterization tests in a wide temperature range

Mechanical properties of hyperelastic materials are often very sensitive to temperature changes. Therefore, material characterization tests of the analyzed hyperelastic target material were carried out in a wide temperature range ($-90\,°C$ to $+100\,°C$). Compression tests were performed at elevated temperatures $40\,°C$ to $+80\,°C$. Based on the results, it can be concluded that the material is very sensitive to temperature rise. As the temperature increased, the material became more plastic and the resistance it exhibited to the punches of the testing machine, and thus, the stresses registered in it decreased. The internal structure of the material was also degraded much earlier, so that the exponential increase in stresses in the material occurred at significantly lower strains than in the case of samples tested at room temperature. The results of quasi-static compression tests of the target material at elevated temperatures are shown in Fig. 11. In Fig. 11, a different way of material failure with increasing temperature can be observed. With the increase in temperature, the processes of degradation of the
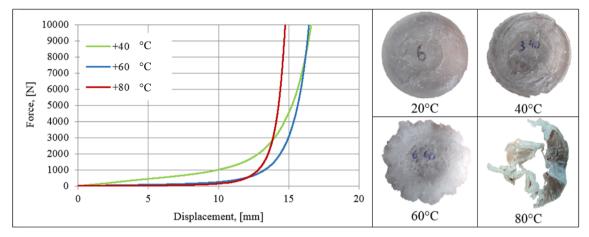
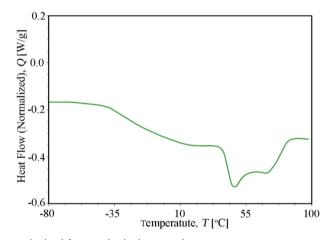**Fig. 11** Results of quasi-static compression tests of the target material at elevated temperatures

Fig. 12 An example DSC curve obtained for samples in the normal state

internal structure of the material were significantly intensified, which resulted in increasingly ragged edges of the samples.

Additional tests were carried out with Differential scanning calorimetry (DSC) method. DSC is a commonly used thermal analysis technique that measures the changes in the physical properties of the sample subjected to thermal heating. During the test, a sample is enclosed inside the pan, which is in the next step mounted inside the furnace on the thermoelectric disk along with an empty reference. The research was conducted in two variants. The first one consisted in determining the parameters characteristic for the sample in the normal state in the range from –90 °C to + 100 °C. During the tests, the glass transition and softening processes were analyzed. In the second variant, preliminary conditioning of the test sample was carried out in the following cycles: 35 °C for 6 h, 40 °C for 6 h, 45 °C for 3 h and 50 °C for 6 h. After conditioning at the specified temperature, the samples were cooled to 0 °C, then heated at a heating rate of 5 °C/min to 100 °C. In this case, only the softening process of the tested samples was analyzed. The results of DSC analyses for the tested samples are shown in Figs. 12 and 13 and in Tables 1 and 2.

Hermetic aluminum pans were used during the tests carried out in a nitrogen atmosphere, with a heating rate of 5 °C/min.

DSC analysis showed that two changes characterized the sample. The first is the glass transition process consisting in the transition from a plastic state to a glass state. The tested material loses its plastic properties at temperature below 0 °C. In addition, it is crucial from the user point of view that in temperature 40 °C, it begins to soften, and this transformation takes place in the wide temperature range. The designated temperature of the end of the softening process is about 85 °C (see Fig. 13). Based on the obtained test results, it can be concluded that tested material retains its functional properties in the temperature range above 0 °C and below 40 °C.
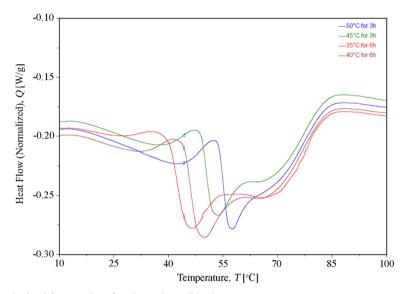
Fig. 13 DSC curves obtained for samples after thermal conditioning

Table 1 DSC results of SEBS in normal condition

Sample no.	Glass transition			Softening			
	T_{onset} (°C)	T_{mid} (°C)	T_{end} (°C)	T_{onset} (°C)	T_{max} (°C)	T_{end} (°C)	Q (J/g)
1gs	-41.6	-19.6	1.0	39.2	47.6	84.3	-31.6
2gs	-41.2	-18.9	1.4	39.6	49.1	85.0	-31.8
3gs	$-40,6$	-17.8	2.2	41.5	51.9	85.8	-31.3

T_{onset}, the temperature at transformation start; T_{max}, temperature at maximum peak, in which the process takes place at the highest rate; T_{mid}, the temperature at which the measured curve is equidistant between the upper and lower tangents; T_{end}, the temperature at the end of transformation; Q, the heat of transformation (J/g)

Table 2 DSC results of SEBS after thermal conditioning

Conditioning model	Sample no.	Softening 1				Softening 2			
		T_{onset} (°C)	T_{max} (°C)	T_{end} (°C)	Q (J/g)	T_{onset} (°C)	T_{max} (°C)	T_{end} (°C)	Q (J/g)
35 °C for 6h	1a	–	–	–	–	40.1	46.7	81.7	-28.5
	2a	–	–	–	–	40.4	47.3	82.8	-29.0
40 °C for 6h	1b	16.0	31.5	39.9	2.1	44.3	50.0	82.5	-24.8
	2b	16.2	31.5	40.0	2.0	44.5	50.4	83.2	-25.1
45 °C for 3h	1c	17.5	36.8	40.6	3.1	49.1	53.8	82.7	-18.8
	2c	17.6	36.7	40.7	3.2	49.0	53.5	82.9	-18.6
50 °C for 3h	1d	18.8	41.3	50.7	5.3	53.8	57.8	81.7	-15.7
	2d	18.6	41.4	50.8	5.2	53.7	58.0	82.2	-15.6

The tests, preceded by preliminary conditioning, showed that heating the samples at a temperature above 40 °C causes the loss of the original thermal properties of the material. As the conditioning temperature increases, the shape of the DSC curve changes and the softening process takes place in two stages. The first softening stage in the case of samples heated at 40 °C, 45 °C and 50 °C will occur below 40 °C. The second softening stage shifts toward higher temperatures as the conditioning temperature increases.

3.4 Compression of projectile at high strain rates

Deformation rates of projectiles under ballistic impact conditions were analyzed in order to properly define numerical model of projectile. During experiments, projectiles fired with different initial velocities (73.4–
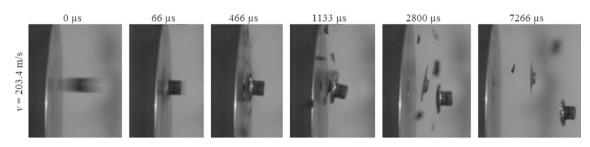
Fig. 14 High-speed camera record of the course of the projectile impact process (impact velocity 203.4 m/s)
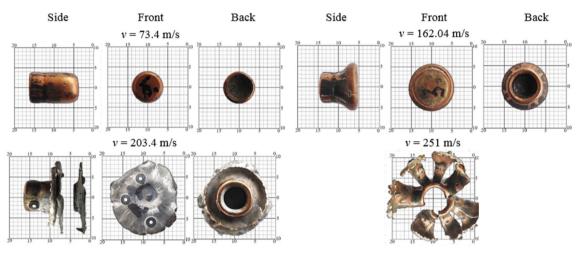

Fig. 15 Deformations of projectiles after impact into rigid target with different velocities

Table 3 Measured values of deformed projectiles dimensions

Impact velocity, v (m/s)	Diameter, D (mm)	Length, L (mm)
Before impact	7.80	13.50
73.40	7.90	12.35
162.04	11.80	10.00
203.40	18.00	9.30

251 m/s) impacted a target much stiffer than them, such that it can be considered rigid (Fig. 14), and their deformations were measured (Fig. 15, Table 3).

4 Material modeling

4.1 Hyperelastic material model parameters identification

Material type *MAT_181_SIMPLIFIED_RUBBER in LS-DYNA software [61,62] was chosen to describe the hyperelastic behavior of target material. Experimentally determined uniaxial engineering stress versus engineering strain constituted main input to the model. Experimental curves should cover both compressive (negative values) and tensile (positive values) regions. Multiple curves can be defined for various values of strain rates and therefore, values of stress at a particular strain and strain rate will be a linear interpolation between these curves (Fig. 16).

The stress–strain curve determined during uniaxial quasi-static compression and tension tests that constituted an input data for the *MAT_181_SIMPLIFIED_RUBBER model in the current work is shown in Fig. 17. Values of additional parameters used in the model are listed in Table 4.
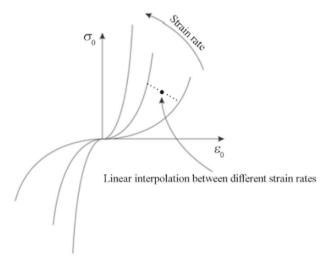
Fig. 16 Typical engineering stress–strain curves for different strain rates used as input in the *MAT_181_SIMPLIFIED_RUBBER in LS-DYNA model
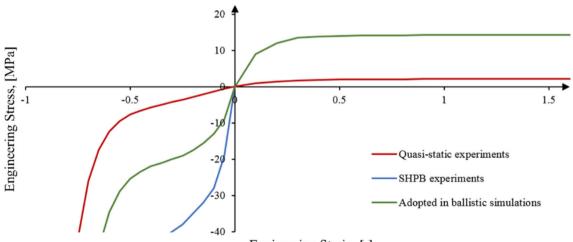
Table 4 Values of parameters in the *MAT_181_SIMPLIFIED_RUBBER for the hyperelastic material

RO (g/cm^3)	KM (MPa)	MU	G	SIGF	PR	SGL	SW	ST	MXEPS
0.95	2000	0.1	500	0.5	0.495	1	1	1	1.5

RO, mass density; *KM*, linear bulk modulus; *MU*, damping coefficient; *G*, shear modulus for frequency independent damping; *SIGF*, limit stress for frequency independent, frictional, damping; *PR*, Poisson ratio; *SGL*, specimen gauge length; *SW*, specimen width; *ST*, specimen thickness; *MXEPS*, maximum principal strain at failure

After defining of the hyperelastic target material model, it was validated by the numerical reproduction of the mechanical tests and comparison of the compression process, deformation of samples and force-displacement curves obtained experimentally and numerically (Figs. 18, 19).

The main attention was paid to compression tests since compressive loads were dominate during the target perforation process simulation of which was the main goal of the study. As it can be seen in Fig. 19, a satisfying agreement in the shapes of the curves obtained experimentally and numerically was obtained. The numerical equivalent of the hyperelastic material was a little bit stiffer than the real material. Similar curves in

Fig. 17 Engineering stress–strain curve determined during uniaxial quasi-static compression and tension tests that constituted an input data for the *MAT_181_SIMPLIFIED_RUBBER model
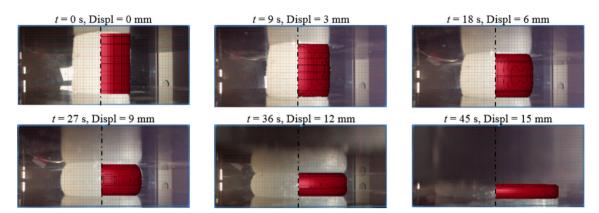
Fig. 18 Deformation of samples obtained experimentally and numerically during hyperelastic material compression tests
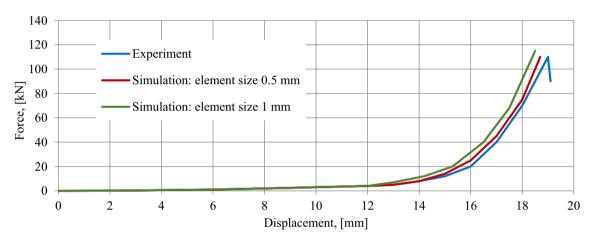

Fig. 19 Comparison of force-displacement curves obtained experimentally and in simulations with the use of determined hyperelastic material model

Table 5 Parameters of the J–C model for simulation components

Material	Density, RO (Tonnes)	Young modulus, E (MPa)	Poisson ratio, PR, (–)	J–C model constants							
				A (MPa)	B (MPa)	n (–)	C (–)	PSFAIL (–)	D_1 (–)	D_2 (–)	D_3 (–)
Jacket	7.85×10^{-9}	210×10^3	0.33	598	575	0.21	0.003	1.15	–	–	–
Steel	7.8×10^{-9}	210×10^3	0.33	1580	756	0.199	0.005	–	0.068	5.32	-2.55
Lead	1.10×10^{-8}	184×10^2	0.42	15	35	0.4	0.003	–	–	–	–

the simulation variants in which elements with the sizes of 0.5 mm and 1 mm were used confirmed very low sensitivity of the model to the mesh size adopted.

4.2 Identification of projectile material model parameters

Metallic components of the simulations were modeled with the Johnson–Cook (J–C) model [61,62]. This elastic–plastic model is highly efficient in reproduction of the metals at high strain rates. It takes into account the effects of strain hardening and thermal softening. Parameters of J–C model for the analyzed components were taken from the literature and from the own library of materials [66,67] and are summarized in Table 5.

A quarter (two symmetry planes) of the model was created. Jacket of the projectile was modeled with 56,653 solid finite elements. Lead core was modeled with elements in Arbitrary Lagrangian–Eulerian (ALE) formulation. The 696,653 elements were used in the whole model including air domain. Validation of the model was based on comparison of deformations of projectiles obtained in simulations and experiments (Fig. 20).
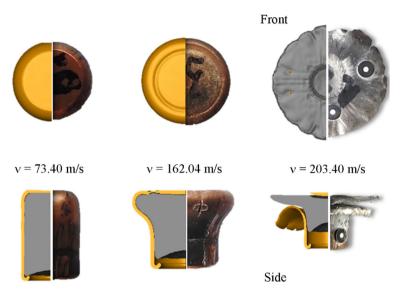
Front

$v = 73.40$ m/s $v = 162.04$ m/s $v = 203.40$ m/s

Side

Fig. 20 Results of validation of the 7.62×25 mm FMJ projectile numerical model (left image—simulation, right image—experiment)

Table 6 Deformations of projectiles obtained in simulations and experiments

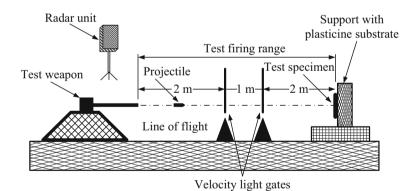| Impact velocity (m/s)	Length of deformed projectile			Diameter of deformed projectile		
	Simulation (mm)	Experiment (mm)	Relative error (%)	Simulation (mm)	Experiment (mm)	Relative error (%)
73.40	11.90	12.35	3.6	7.87	7.90	0.4
162.04	9.73	10.00	2.7	12.00	11.80	1.7
203.40	8.50	9.30	8.6	18.80	18.00	4.4

Fig. 21 Ballistic impact tests stand

Small differences (measured by the relative error value) between experimental and numerical results were observed (Table 6). The error did not exceed 13%. It confirmed that the model was properly defined.

5 Ballistic impact experiments

Ballistic impact tests were carried out on the stand presented in Fig. 21. Several variants of target thicknesses were subjected to projectile impact. The edges of the sample were fixed by the frame tightened with screws. The impact and residual velocities of projectiles were measured with optical gates and Doppler radar (Weibel model SL-520P), respectively. Three shots were performed for each of the target thicknesses.

The results of the experiments are shown in Table 7 and in Fig. 22.

Table 7 Results of ballistic impact experiments (average value from 3 trials)

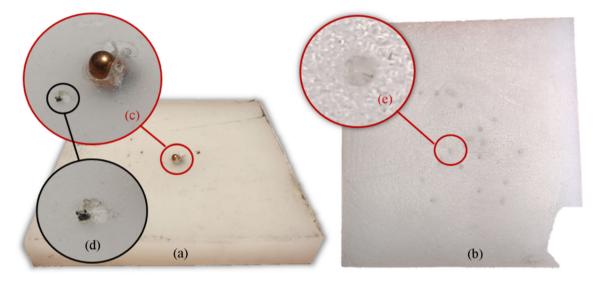| Target thickness (mm)	0	10	20	30	80	140	180	220
Residual velocity of projectile (m/s)	450	441.5	432.8	426.4	373.2	124.3	45.6	0

Fig. 22 Results of experimental tests: **a** target surface on the outlet side; **b** target surface on the inlet side; **c** projectile stuck in the target; **d** outlet hole; **e** inlet hole
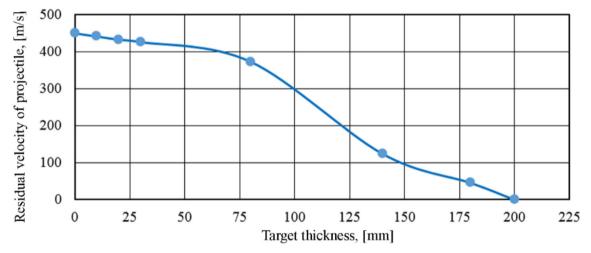

Fig. 23 Results of experimental tests: residual velocity of projectiles in function of target thickness

During the experiments, the high elastic recovery properties of the target material were observed. The projectile remained undeformed during the perforation process of the hyperelastic material.

The dependence between the target thickness and the residual velocity of projectile is shown in Fig. 23. It is difficult to distinguish whether the trend is more linear or exponential especially due to the results obtained for the 80-mm and 140-mm-thick target. The projectile was stopped by the 220-mm-thick target and in that case the depth of penetrations was equal DP = 200 mm. Beside the indication of the target energy absorption and dissipation properties, these data were used for validation of the numerical equivalent of the hyperelastic material. The dependence was used also for determination of the material strain-rate hardening properties, because results from SHPB experiments were unreliable.
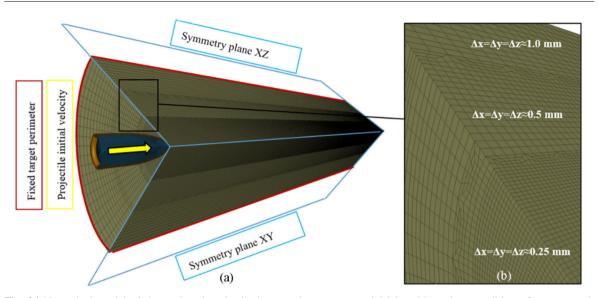
Fig. 24 Numerical model of the analyzed projectile impact phenomenon: **a** initial and boundary conditions; **b** target mesh refinement method

6 Ballistic impact simulations

Simulations reproducing ballistic impact experiments were carried as a final validation of the hyperelastic target material model. A three-dimensional (3D) (with two symmetry planes) numerical model of the analyzed phenomenon of 7.62×25 mm FMJ projectile impact into hyperelastic rubber target was modeled (Fig. 24). The target layers were fixed around the perimeter. The elements size in the projectile impact zone was 0.25 mm (Fig. 24b).

In the simulations, the thickness of the target was a variable parameter. It was changed from 10 to 220 mm similar like in experiments. In consequence, the number of finite elements used for modeling of the components also varied and equaled from 111,224 to 1,446,824 for the targets with the thickness of 10 mm and 220 mm, respectively. Contacts between the simulation components described in the Lagrange formulation were realized using the *CONTACT_ERODING_SINGLE_SURFACE algorithm. The friction between components was included in the calculations. In the LS-Dyna®software, it is defined with the following equation [61,62]:

$$\mu = \text{FD} + (\text{FS} - \text{FD})e^{-\text{DC}|v_{\text{rel}}|} \tag{1}$$

where FS, FD—static and kinematic friction coefficient, respectively, v_{rel}—relative velocity between two surfaces in contact, DC—decay constant.

The values of the friction coefficients were adopted on the basis of the literature data [68–71] and for the steel-rubber pair equaled: FS $= 0.7$, FD $= 0.25$ and DC was adopted as 0.00001 what gives the relation between friction coefficient and relative velocity presented in Fig. 25.

The results of simulation of projectile penetration into the hyperelastic target were presented in the form of deformations of the components at different time of the penetration process in Figs. 26, 27, 28 and 29.

The example of the shape penetration crater in the stack of rubber plates with a total thickness of 180 mm at different time is shown in Fig. 26. The initially defined values of parameters in the constitutive equations of the hyperelastic target (Sect. 4.1) were tuned in order to obtain the shape of the numerical curve of projectile residual velocity in function of target thickness as close as those observed in experiments (Fig. 23).

Although some differences between the experimental and numerical curves can be noticed, the general trend provides satisfying agreement (Fig. 27).

The largest difference between simulation and experiments was noticed for the 140- mm-thick target and equaled $\Delta = 15\%$. Moreover, the determined parameters of the hyperelastic target material provide satisfying reproduction of the characteristic elastic recovery of the material (Fig. 28). The diameter of the final penetration crater in the perforated targets ($\Phi = 2.3$ mm) was significantly smaller than the diameter of maximum temporal cavity as well as the diameter of the projectile (7.62×25 mm). This effect is shown in Fig. 29. As can be seen from the analysis of points A and B for these points, the radius of the temporary cavity is between 4.5 and 5 mm, which correlates with the data presented in Fig. 28.
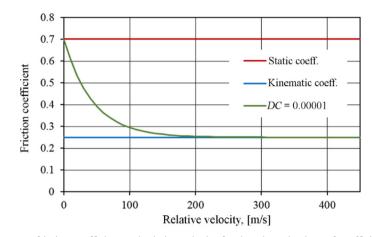
Fig. 25 Dependence between friction coefficient and relative velocity for the adopted values of coefficients and decay constant
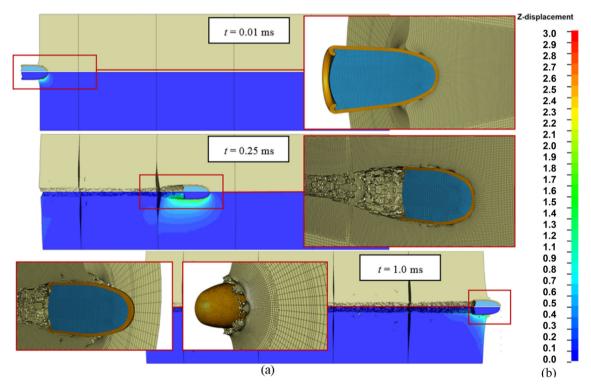

Fig. 26 Results of simulation of projectile penetration into the 180- mm-thick hyperelastic target: **a** penetration crater at different stages of perforation process and **b** Z–displacement of target elements indicating elastic recovery of target

The model sensitivity to adopted methods of target discretization (mesh density), target failure criteria and values of friction coefficients was analyzed. Therefore, simulations for the 180 mm thick target in which various mesh sizes, friction coefficients as well as values of limiting principal strains (erosion) in the target material model were carried out (Fig. 30).

The model is relatively sensitive to the changes of the values of failure criterion parameter—maximum principal strain (MXEPS) in the range of 1.0-−1.75. The initial value of a failure criterion based on maximum principal strain MXEPS = 1.5 was adopted on the basis of experimental tension tests in which the sample was damaged at the engineering strain equal 150%. Increasing the MXEPS for the hyperelastic target material by 17% from the value of MXEPS = 1.5 to MXEPS = 1.75 caused premature termination of calculation by highly distorted elements and negative volume error. When the MXEPS was reduced by 33% from the value of MXEPS = 1.5 to MXEPS = 1.0, the residual velocity of projectile increased from the value of 46 m/s to the value of 158 m/s. Since the percent of eroded elements in all variants of calculation was similar, the growth
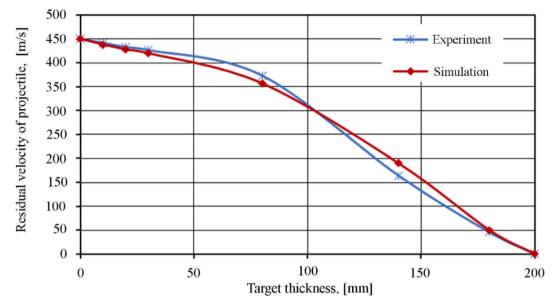
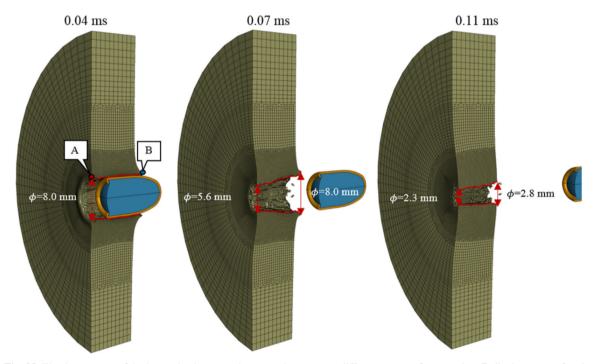**Fig. 27** An experimental and numerical curves in residual velocity in function thickness of samples

Fig. 28 Elastic recovery of the hyperelastic target: **A** penetration crater at different stages of penetration; **B** displacement of nodes lying on the edge of the penetration craters in time

of the residual velocity of projectile together with the decrease of the MXEPS value was a consequence of the fact that target elements eroded earlier instead of erosion of greater number of elements.

The mesh size in the analyzed range (sizes of the mesh of elements located in the area of direct impact of projectile $\Delta x = \Delta y = \Delta z = 0.5$ mm and $\Delta x = \Delta y = \Delta z = 0.25$ mm) does not significantly affect the results (Fig. 31b). Additionally, time required to finish the computation increased from 3 to 21 h what makes mesh refinement pointless.

Determined numerical model exhibits also a relatively high sensitivity to the values of adopted friction parameters. In the analyzed variants, the coefficients of static and dynamic friction coefficients were constant
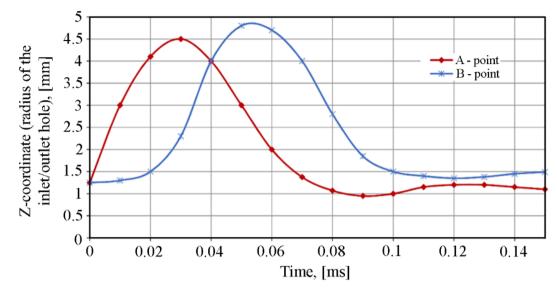
Fig. 29 Displacement of nodes lying on the edges of the penetration craters in time
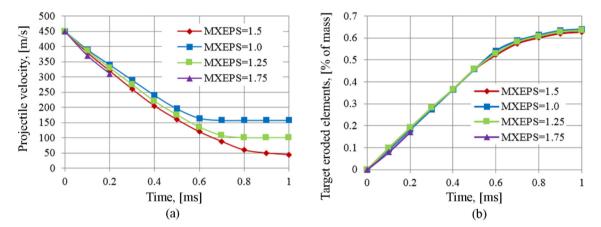

Fig. 30 Dependence between the value of MXEPS in the target on: **a** residual velocity of projectile; **b** target erosion ratio expressed in percent of mass
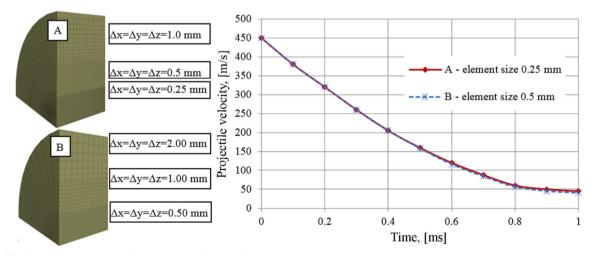

Fig. 31 Mesh sensitivity of the model—influence of target mesh size on the projectile residual velocity
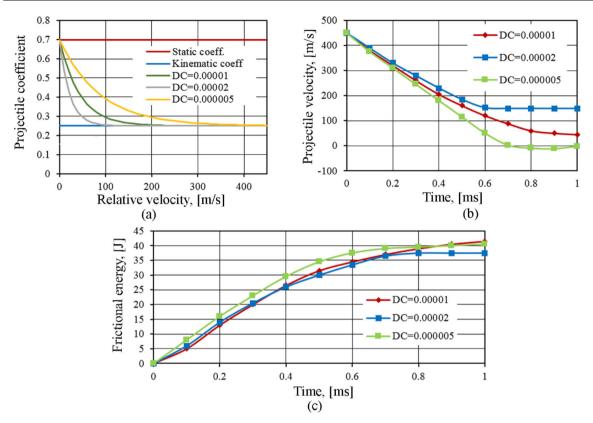
Fig. 32 Friction sensitivity of the model: **a** relation between friction coefficients values and relative velocity of contacting surfaces for the adopted DC values; **b** projectile velocity in time for different values of DC; **c** frictional energy in time for different values of DC

and equaled FS = 0.7 and FD = 0.25, respectively. However, the value of the decay constant (DC) defining the way of transition from the static to dynamic friction (dependence between the friction coefficient and the relative velocity of contacting surfaces) was changed (Fig. 32a). As it can be seen in Fig. 32b, when the DC was changed by 100% from the initial value of DC = 0.00001 to DC = 0.00002, the residual velocity of projectile after perforation of target increased from v_r = 45 m/s to v_r = 150 m/s. On the other hand, when the DC was decreased to value of DC = 0.000005, the higher values of friction coefficients were obtained at the earlier stages of perforation, projectile deceleration was more intensive and in consequence the projectile was stopped in the target. It was confirmed on the graph presenting frictional energy in time for the penetration process. The curve for the DC = 0.000005 increases the most intensively, up to the point when the projectile is stopped in the target (Fig. 32c).

7 Conclusions

Conclusions that can be drawn on the basis of performed experimental and numerical analyses are as follows:

1. Mechanical properties of the hyperelastic material were determined in a wide range of strain rates and temperatures.
2. The analyzed hyperelastic material showed very high temperature sensitivity. Its mechanical properties start to decrease as the temperature exceed 40°C.
3. An accurate and verified constitutive model of novel hyperelastic material was defined on the basis of experimental mechanical and ballistic tests.
4. The model will facilitate designing processes of various types of protective structures used in different ballistic applications including layers of composite armors, projectile catching systems and anti-ricochet layers covering walls of shooting ranges, ballistic tunnels, etc.
5. Defined material model of hyper-elastic target was validated against experimental data. Satisfying agreement was obtained. The general trends of the plots of projectile residual velocities in function of target

thickness was similar; however, for the 140-mm-thick target the maximum difference was noticed that equaled about 15%. The use of the tested hyperelastic target material to slow down more energetic projectiles, e.g., 7.62×51 mm, may be promising; however, it requires confirmation by experiment.

6. The determined parameters of the hyperelastic target material provide satisfying reproduction of the characteristic elastic recovery of the material. The diameter of the final penetration crater in the perforated targets ($\Phi = 2.3$ mm) was significantly smaller than the diameter of maximum temporal cavity as well as the diameter of the projectile (7.62×25 mm).

7. Maximum principal strain MXEPS $= 1.5$ was adopted as a target failure criterion on the basis of experimental tension tests in which the sample was damaged at the engineering strain equal 150%. However, when the MXEPS was reduced by 33% from the value of MXEPS $= 1.5$ to MXEPS $= 1.0$, the residual velocity of projectile increased from the value of 46 m/s to the value of 158 m/s.

8. When the decay constant in the friction definition was changed by 100% from the initial value of DC $= 0.00001$ to DC $= 0.00002$, the residual velocity of projectile after perforation of target increased from $v_r = 45$ m/s to $v_r = 150$ m/s. On the other hand, when the DC was decreased to value of DC $= 0.000005$, the higher values of friction coefficients were obtained at the earlier stages of perforation, projectile deceleration was more intensive and in consequence the projectile was stopped in the target.

9. Determined parameters of numerical model are valid only for the analyzed case (mesh size, friction, failure criteria), and special attention must be paid when some changes are incorporated. Future works will be focused on decreasing the model sensitivity to the analyzed parameters, as well as on limiting the number of parameters that were adjusted in order to obtain the desired results by performing of appropriate experiments.

Declarations

Conflict of interest The authors declare no conflicts of interest.

Institutional review board statement Not applicable.

Informed consent statement Not applicable.

Data availability Data sharing is not applicable to this article.

Author contributions PZ contributed to conceptualization, methodology, investigation, software, and writing—original draft preparation. MC contributed to visualization, writing—reviewing and editing, and funding acquisition. KS contributed to investigation, data curation, and formal analysis. JM contributed to investigation, data curation, and formal analysis. MB contributed to methodology, formal analysis, resources, and data curation. EB contributed to writing—reviewing and editing. RG contributed to formal analysis, and writing—reviewing and editing. MM contributed to validation, resources, methodology, data curation, visualization, and project administration. DP contributed to software, writing—Original draft preparation, and investigation. MB contributed to software, visualization, and data curation. KJ contributed to writing—original draft preparation, investigation, visualization, and supervision. RG contributed to investigation, data curation, and formal analysis. PP contributed to investigation, data curation, and formal analysis.

References

1. Pouriayevali, H., Guo, Y.B., Shim, V.P.W.: A visco-hyperelastic constitutive description of elastomer behaviour at high strain rates. Procedia Eng. **10**, 2274–2279 (2011). https://doi.org/10.1016/j.proeng.2011.04.376

2. Yang, H., Yao, X., Zheng, Z., Gong, L., Yuan, L., Yuan, Y., Liu, Y.: Highly sensitive and stretchable graphene-silicone rubber composites for strain sensing. Compos. Sci. Technol. **167**, 371–378 (2018). https://doi.org/10.1016/j.compscitech.2018.08.022

3. Tubaldi, E., Mitoulis, S.A., Ahmadi, H.: Comparison of different models for high damping rubber bearings in seismically isolated bridges. Soil Dyn. Earthq. Eng. **104**, 329–345 (2018). https://doi.org/10.1016/j.soildyn.2017.09.017

4. Yang, H., Yao, X.-F., Wang, S., Ke, Y.-C., Huang, S.-H., Liu, Y.-H.: Analysis and inversion of contact stress for the finite thickness Neo-Hookean layer. J. Appl. Mech. (2018). https://doi.org/10.1115/1.4040598

5. Appleby-Thomas, G.J., Wood, D.C., Hameed, A., Painter, J., Le-Seelleur, V., Fitzmaurice, B.C.: Investigation of the high-strain rate (shock and ballistic) response of the elastomeric tissue simulant Perma-Gel®. Int. J. Impact Eng. **94**, 74–82 (2016). https://doi.org/10.1016/j.ijimpeng.2016.04.003

6. Stopforth, R., Adali, S.: Experimental study of bullet-proofing capabilities of Kevlar, of different weights and number of layers, with 9 mm projectiles. Def. Technol. **15**, 186–192 (2019). https://doi.org/10.1016/j.dt.2018.08.006

7. Bocian, M., Jamroziak, K., Kulisiewicz, M., Pach, J,, Pyka, D.: Numerical study of dynamic properties of a selected material layer of bulletproof shields. EASD Procedia pp. 265–272 (2020). https://doi.org/10.47964/1120.9021.19238

8. Burian, W., et al.: Finite element modeling of ballistic inserts containing aramid fabrics under projectile impact conditions: comparison of methods. Compos. Struct. **294**, 115752 (2022). https://doi.org/10.1016/j.compstruct.2022.115752

9. Zochowski, P., Bajkowski, M., Grygoruk, R., et al.: Comparison of numerical simulation techniques of ballistic ceramics under projectile impact conditions. Materials **15**(1), 18 (2022). https://doi.org/10.3390/ma15010018

10. Wisniewski, A., et al.: Anti-trauma pads based on non-Newtonian materials for flexible bulletproof inserts. In: Proceedings—29th International Symposium on Ballistics, BALLISTICS 2016, vol. 2, pp. 2034–2045 (2016). ISBN: 978-160595317-5

11. Leonowicz, M., et al.: Optimization of the material systems with magnetorheological fluids. In: Proceedings—28th International Symposium on Ballistics, BALLISTICS 2014, vol. 2, pp. 1602–1612 (2014). ISBN 978-160595149-2

12. Wisniewski, A., et al.: Optimization of the material systems with shear-thickening fluids. In: Proceedings—28th International Symposium on Ballistics, BALLISTICS 2014, vol. 2, pp. 1613–1622 (2014). ISBN 978-160595149-2

13. dell'Isola, F., Seppecher, P., Alibert, J.J., Lekszycki, T., Grygoruk, R., Pawlikowski, M., Steigmann, D., et al.: Pantographic metamaterials: an example of mathematically driven design and of its technological challenges. Contin. Mech. Thermodyn. **31**(4), 851–884 (2019)

14. dell'Isola, F., Seppecher, P., Spagnuolo, M., Barchiesi, E., Hild, F., Lekszycki, T., Giorgio, I., et al.: Advances in pantographic structures: design, manufacturing, models, experiments and image analyses. Contin. Mech. Thermodyn. **31**(4), 1231–1282 (2019)

15. Stilz, M., dell'Isola, F., Giorgio, I., Eremeyev, V.A., Ganzenmüller, G., Hiermaier, S.: Continuum models for pantographic blocks with second gradient energies which are incomplete. Mech. Res. Commun. **125**, 103988 (2022)

16. Alibert, J.J., Seppecher, P., dell'Isola, F.: Truss modular beams with deformation energy depending on higher displacement gradients. Math. Mech. Solids **8**(1), 51–73 (2003)

17. Yildizdag, M.E., Ciallella, A., D'Ovidio, G.: Investigating wave transmission and reflection phenomena in pantographic lattices using a second-gradient continuum model. Math. Mech. Solids (2022). https://doi.org/10.1177/10812865221136250

18. Karl, J., Kirsch, F., Faderl, N., Perko, L., Fras, T.: Optimizing viscoelastic properties of rubber compounds for ballistic applications. Appl. Sci. (2020). https://doi.org/10.3390/app10217840

19. Roland, C.M., Fragiadakis, D., Gamache, R.M.: Elastomer-steel laminate armor. Compos. Struct. **92**, 1059–1064 (2010). https://doi.org/10.1016/j.compstruct.2009.09.057

20. Sakamoto, M.: Experimental validation of the butyl-rubber finite element (FE) material model for the blast-mitigating floor mat (2015)

21. Baranowski, P., Małachowski, J., Mazurkiewicz, Ł: Local blast wave interaction with tire structure. Def. Technol. **16**, 520–529 (2020). https://doi.org/10.1016/j.dt.2019.07.021

22. Williams, A.G., Dhingra, J.: IHSTM Jane's® Weapons: Ammunition. IHS JANES, London (2016)

23. Motyl, K., Zygmunt, B., Magier, M., Borkowski, J.: Theoretical and experimental research of anti-tank kinetic penetrator ballistics. Bull. Pol. Acad. Sci. Tech. Sci. **65**, 399–404 (2017). https://doi.org/10.1515/bpasts-2017-0045

24. Magier, M.: The conception of the segmented kinetic energy penetrators for tank guns. J. Appl. Mech. (2010). https://doi.org/10.1115/1.4001714

25. Żochowski, P., Warchoł, R., Miszczak, M., Nita, M., Pankowski, Z., Bajkowski, M.: Experimental and numerical study on the PG-7VM warhead performance against high-hardness armor steel. Materials (2021). https://doi.org/10.3390/ma14113020

26. Pyka, D., Kurzawa, A., Bocian, M., Bajkowski, M., Magier, M., Sliwinski, J., Jamroziak, K.: Numerical and experimental studies of the Łk type shaped charge. Appl. Sci. (Switz.) **10**, 1–20 (2020). https://doi.org/10.3390/app10196742

27. Carleone, J.: Tactical Missile Warheads. American Institute of Aeronautics and Astronautics Inc., Reston (1993)

28. Held, M.: Fundamentals of shaped charges. Walters, William P., Zukas, Jonas A.: John Wiley & Sons, New York 1989, 398 pp., 84 Figs., Price: $85, ISBN 0-471-62172-2. Propellants Explos. Pyrotech. **14**, 220 (1989). https://doi.org/10.1002/prep.19890140510

29. Fras, T.: Experimental and numerical study on a non-explosive reactive armour with the rubber interlayer applied against kinetic-energy penetrators-the 'bulging effect' analysis. Materials (2021). https://doi.org/10.3390/ma14123334

30. Shepherd, C.J., Appleby-Thomas, G.J., Hazell, P.J., Allsop, D.F.: The dynamic behaviour of ballistic gelatin. AIP Conf. Proc. **1195**, 1399–1402 (2009). https://doi.org/10.1063/1.3295071

31. Appleby-Thomas, G.J., Hazell, P.J., Wilgeroth, J.M., Shepherd, C.J., Wood, D.C., Roberts, A.: On the dynamic behavior of three readily available soft tissue simulants. J. Appl. Phys. **109**, 84701 (2011). https://doi.org/10.1063/1.3573632

32. Shepherd, C.J., Appleby-Thomas, G.J., Wilgeroth, J.M., Hazell, P.J., Allsop, D.F.: On the response of ballistic soap to one-dimensional shock loading. Int. J. Impact Eng. **38**, 981–988 (2011). https://doi.org/10.1016/j.ijimpeng.2011.07.003

33. Ndompetelo, N., Viot, P., Dyckmans, G., Chabotier, A.: Numerical and experimental study of the impact of small caliber projectiles on ballistic soap. J. Phys. IV **134**, 385–390 (2006). https://doi.org/10.1051/jp4:2006134059

34. Swain, M.V., Kieser, D.C., Shah, S., Kieser, J.A.: Projectile penetration into ballistic gelatin. J. Mech. Behav. Biomed. Mater. **29**, 385–392 (2014). https://doi.org/10.1016/j.jmbbm.2013.09.024

35. Bresson, F., Ducouret, J., Peyré, J., Maréchal, C., Delille, R., Colard, T., Demondion, X.: Experimental study of the expansion dynamic of 9mm Parabellum hollow point projectiles in ballistic gelatin. Forensic Sci. Int. **219**, 113–118 (2012). https://doi.org/10.1016/j.forsciint.2011.12.007

36. Luo, S., Xu, C., Chen, A., Zhang, X.: Experimental investigation of the response of gelatine behind the soft body armor. Forensic Sci. Int. **266**, 8–13 (2016). https://doi.org/10.1016/j.forsciint.2016.04.019

37. Liu, L., Fan, Y., Li, W.: Viscoelastic shock wave in ballistic gelatin behind soft body armor. J. Mech. Behav. Biomed. Mater. **34**, 199–207 (2014). https://doi.org/10.1016/j.jmbbm.2014.02.011

38. Giorgio, I., Spagnuolo, M., Andreaus, U., Scerrato, D., Bersani, A.M.: In-depth gaze at the astonishing mechanical behavior of bone: a review for designing bio-inspired hierarchical metamaterials. Math. Mech. Solids **26**(7), 1074–1103 (2021)

39. Giorgio, I., De Angelo, M., Turco, E., Misra, A.: A Biot–Cosserat two-dimensional elastic nonlinear model for a micromorphic medium. Contin. Mech. Thermodyn. **32**(5), 1357–1369 (2020)

40. Cronin, D.S., Falzon, C.: Characterization of 10% ballistic gelatin to evaluate temperature, aging and strain rate effects. Exp. Mech. **51**, 1197–1206 (2011). https://doi.org/10.1007/s11340-010-9438-z

41. Fackler, M.L., Malinowski, J.A.: Ordnance gelatin for ballistic studies: detrimental effect of excess heat used in gelatin preparation. Am J Forensic Med Pathol **9**(3), 218–219 (1988)

42. Mrozek, R.A., Leighliter, B., Gold, C.S., Beringer, I.R., Yu, J.H., VanLandingham, M.R., Moy, P., Foster, M.H., Lenhart, J.L.: The relationship between mechanical properties and ballistic penetration depth in a viscoelastic gel. J. Mech. Behav. Biomed. Mater. **44**, 109–120 (2015). https://doi.org/10.1016/j.jmbbm.2015.01.001

43. Mauzac, O., Paquier, C., Debord, E., Barbillon, F., Mabire, P., Jacquet, J.: A substitute of gelatin for the measurement of dynamic back face deformation. In Personal armour systems symposium (Quebec: IPAC), Canada, pp. 1–10 (2010)

44. Mabbott, A., Carr, D.J., Champion, S., Malbon, C., Tichler, C.: Comparison of 10 % gelatine, 20 % gelatine and Perma-Gel for ballistic testing (2013)

45. Kalcioglu, Z.I., Qu, M., Strawhecker, K.E., Shazly, T., Edelman, E., VanLandingham, M.R., Smith, J.F., Van Vliet, K.J.: Dynamic impact indentation of hydrated biological tissues and tissue surrogate gels. Philos. Mag. **91**, 1339–1355 (2011). https://doi.org/10.1080/14786435.2010.512574

46. Bracq, A., Haugou, G., Delille, R., Lauro, F., Roth, S., Mauzac, O.: Experimental study of the strain rate dependence of a synthetic gel for ballistic blunt trauma assessment. J. Mech. Behav. Biomed. Mater. **72**, 138–147 (2017). https://doi.org/10.1016/j.jmbbm.2017.04.027

47. Giorgio, I.: A variational formulation for one-dimensional linear thermo-viscoelasticity. Math. Mech. Complex Syst. **9**(4), 397–412 (2021). https://doi.org/10.2140/memocs.2021.9.397

48. Andreaus, U., Chiaia, B., Placidi, L.: Soft-impact dynamics of deformable bodies. Contin. Mech. Thermodyn. **25**(2), 375–398 (2013)

49. Placidi, L., Barchiesi, E., Misra, A.: A strain gradient variational approach to damage: a comparison with damage gradient models and numerical results. Math. Mech. Complex Syst. **6**(2), 77–100 (2018)

50. Placidi, L., Misra, A., Barchiesi, E.: Two-dimensional strain gradient damage modeling: a variational approach. Z. Angew. Math. Phys. **69**(3), 1–19 (2018)

51. Placidi, L., Barchiesi, E.: Energy approach to brittle fracture in strain-gradient modelling. Proc. R. Soc. A Math. Phys. Eng. Sci. **474**(2210), 20170878 (2018)

52. Abali, B.E., Klunker, A., Barchiesi, E., Placidi, L.: A novel phase-field approach to brittle damage mechanics of gradient metamaterials combining action formalism and history variable. ZAMM J. Appl. Math. Mech. **101**(9), e202000289 (2021)

53. Ciallella, A., Scerrato, D., Spagnuolo, M., Giorgio, I.: A continuum model based on Rayleigh dissipation functions to describe a Coulomb-type constitutive law for internal friction in woven fabrics. Z. Angew. Math. Phys. **73**(5), 1–17 (2022)

54. Abali, B.E., Vazic, B., Newell, P.: Influence of microstructure on size effect for metamaterials applied in composite structures. Mech. Res. Commun. **122**, 103877 (2022)

55. Barchiesi, E., Spagnuolo, M., Placidi, L.: Mechanical metamaterials: a state of the art. Math. Mech. Solids **24**(1), 212–234 (2019)

56. Bracq, A., Haugou, G., Bourel, B., Maréchal, C., Lauro, F., Roth, S., Mauzac, O.: On the modeling of a visco-hyperelastic polymer gel under blunt ballistic impacts. Int. J. Impact Eng. **118**, 78–90 (2018). https://doi.org/10.1016/j.ijimpeng.2018.04.001

57. Fontenier, B., Hault-Dubrulle, A., Drazetic, P., Fontaine, C., Naceur, H.: On the mechanical characterization and modeling of polymer gel brain substitute under dynamic rotational loading. J. Mech. Behav. Biomed. Mater. **63**, 44–55 (2016). https://doi.org/10.1016/j.jmbbm.2016.06.008

58. Azar, F.S., Metaxas, D.N., Miller, R.T., Schall, M.D.: Methods for predicting mechanical deformations in the breast during clinical breast biopsy. In: Proceedings of the IEEE 26th Annual Northeast Bioengineering Conference (Cat. No. 00CH37114), pp. 63–64 (2000). https://doi.org/10.1109/NEBC.2000.842380

59. Cronin, D.S.: Ballistic gelatin characterization and constitutive modeling BT: dynamic behavior of materials. In: Proulx, T. (ed.), vol. 1, pp. 51–55. Springer, New York (2011)

60. Kneubuehl, B.P.: Ballistic Protection. Swiss Defense Procurement Agency, Thun (2003)

61. Livermore Software Technology Corporation (LSTC): LS-DYNA R12 Kewword User's Manual, vol. I (2020)

62. Manual, K.U.S., Ii, V.: Keyword User ' S Manual, vol. Ii (2012)

63. Panowicz, R., Janiszewski, J.: Tensile split Hopkinson bar technique: numerical analysis of the problem of wave disturbance and specimen geometry selection. Metrol. Meas. Syst. **23**, 425–436 (2016). https://doi.org/10.1515/mms-2016-0027

64. Baranowski, P., Malachowski, J., Gieleta, R., Damaziak, K., Mazurkiewicz, L., Kołodziejczyk, D.: Numerical study for determination of pulse shaping design variables in SHPB apparatus. Bull. Pol. Acad. Sci. Tech. Sci. **61**, 459–466 (2013). https://doi.org/10.2478/bpasts-2013-0045

65. Baranowski, P., Gieleta, R., Malachowski, J., Damaziak, K., Mazurkiewicz, L.: Split Hopkinson pressure bar impulse experimental measurement with numerical validation. Metrol. Meas. Syst. (2014). https://doi.org/10.2478/mms-2014-0005

66. Carbajal, L., Jovicic, J., Kuhlmann, H.: Assault riffle bullet-experimental characterization and computer (FE) modeling BT: experimental and applied mechanics. In: Proulx, T. (ed.), vol. 6, pp. 651–668. Springer, New York(2011)

67. Zochowski, P., Bajkowski, M., Grygoruk, R., Magier, M., Burian, W., Pyka, D., Bocian, M., Jamroziak, K.: Ballistic impact resistance of bulletproof vest inserts containing printed titanium structures. Metals (2021). https://doi.org/10.3390/met11020225

68. https://www.teachengineering.org/content/nyu_/activities/nyu_heavy/nyu_heavy_activity1_coftable.pdf. Coefficient of friction. Accessed 8 Jan 2021

69. https://www.tribology-abc.com/abc/cof.html. Coefficient of friction. Accessed 8 Jan 2021

70. Ciornei, F.C., Alaci, S., Ciogole, V.I., Ciornei, M.C.: Valuation of coefficient of rolling friction by the inclined plane method. IOP Conf. Ser. Mater. Sci. Eng. **200**, 12006 (2017). https://doi.org/10.1088/1757-899x/200/1/012006

71. Saenmuangchin, R., Techarang, T., Mekprayoon, S., Zulfah, N.L., Siripinyanond, A. Chapter 7: field-flow fractionation. In: D.B.T.-S.I.S. in I., Beauchemin, I., (eds.), Elsevier, Amsterdam, pp. 357–380 (2020). https://doi.org/10.1016/B978-0-444-59482-2.00007-5